

A combined experimental and numerical study on the plastic damage in microalloyed Q345 steels

Bin Li^a and Changwen Mi*

*Jiangsu Key Laboratory of Engineering Mechanics, School of Civil Engineering, Southeast University,
Nanjing, Jiangsu 210096, China*

(Received December 26, 2018, Revised May 9, 2019, Accepted June 2, 2019)

Abstract. Damage evolution in the form of void nucleation, propagation and coalescence is the primary cause that is responsible for the ductile failure of microalloyed steels. The Gurson-Tvergaard-Needleman (GTN) damage model has proven to be extremely robust for characterizing the microscopic damage behavior of ductile metals. Nonetheless, successful applications of the model on a given metal type are limited by the correct identification of damage parameters as well as the validation of the calculated void growth rate. The purpose of this study is two-fold. First, we aim to identify the damage parameters of the GTN model for Q345 steel (Chinese code), due to its extensive application in mechanical and civil industries in China. The identification of damage parameters is facilitated by the well-suited response surface methodology, followed by a complete analysis of variance for evaluating the statistical significance of the identified model. Second, taking notched Q345 cylinders as an example, finite element simulations implemented with the identified GTN model are performed in order to analyze their microscopic damage behavior. In particular, the void growth rate predicted from the simulations is successfully correlated with experimentally measured acoustic emissions. The quantitative correlation suggests that during the yielding stage the void growth rate increases linearly with the acoustic emissions, while in the strain-hardening and softening period the dependence becomes an exponential function. The combined experimental and finite element approach provides a means for validating simulated void growth rate against experimental measurements of acoustic emissions in microalloyed steels.

Keywords: plastic damage; acoustic emission; parameter identification; SEM morphology; microalloyed Q345 steel

1. Introduction

As one of the primary construction materials, microalloyed steel is widely used for manufacturing vessels, bridges, ships and hoisting machines. These components and structures are subjected to a variety of loading conditions including both monotonic and cyclic forces. The major failure mechanism can be attributed to the successive accumulation of plastic deformations under elevated external loads, resulting from the continuous nucleation, propagation and coalescence of microvoids (Zhang 2010, Mi 2011, Zanganeh 2013). Ductile damage and microstructural degradation inevitably result in the strength weakening and threaten the structural integrity of mechanical components. It is therefore of importance to develop microscopic damage models for effectively monitoring and characterizing the microscopic damage evolution in ductile metals.

In the past five decades, extensive efforts have been made on developing micromechanical models that are able to effectively describe the ductile failure mechanism of metals. As one of the pioneers, McClintock (1968) proposed

the first analytical model for modeling the growth of isolated cylindrical voids in a rigid perfectly plastic solid. The corresponding model for dilute spherical voids embedded in an infinitely extended matrix was shortly developed by Rice (1969). Both models investigated the effects of stress triaxiality and plastic strain on the ductile growth of voids in infinite solids. However, the Rice-Tracey model of void growth was established without taking into account the effects of matrix boundary, the possible interactions among adjacent voids, and the strain-hardening and softening behavior (Mi 2011). These obvious limitations prevented the Rice-Tracey damage model from extensive applications. More sophisticated damage models were continuously proposed to overcome these issues. For example, Gurson (1977) successfully developed the yield function of plastic deformation for a cylindrical or spherical void embedded in a matrix of finite size. Nonetheless, no attention was given to the acceleration of void growth rate due to the effects of void coalescence under elevated external loading. In other words, the original Gurson's damage model is only concerned with the evolution of the overall void volume fraction, accommodating neither the probability distribution of voids nor the strain hardening and softening effects.

To take into account the adverse effects of microscopic damage events such as void coalescence and localized microyielding on void growth, Tvergaard (1984) further improved the yield function of Gurson's model. In the

*Corresponding author, Ph.D., Professor

E-mail: mi@seu.edu.cn

^a Ph.D. Student

E-mail: libin093@126.com

literature, the modified yield function is generally referred to as the Gurson-Tvergaard-Needleman (GTN) damage model. When compared with its original version, the GTN damage model is much more complicated. A total number of thirteen material parameters is included, being divided into three groups. The first of which is dedicated to model the elastic and plastic properties of the virgin (unvoided) metals. The second group contains three model correction parameters. Six damage parameters form the last group and aim to describe the temporal evolution of void volume fraction in a ductile metal. Provided that all model parameters are well identified, predictions by the GTN damage model have proven to agree with experimental data much better than those of the original Gurson's one. One of the primary causes of the better agreement is of course due to the introduction of a large number of model parameters. In the original Gurson's damage model, there are only two parameters, i.e. the yield or flow stress of the unvoided material and the void volume fraction ratio.

As in the case with any empirical models, the thirteen material parameters of the GTN damage model must be correctly identified before it can be used for modeling the damage evolution in a ductile metal. A few approaches for identifying the GTN model parameters exist in the literature, including the inverse approach (Springmann 2006), the direct current potential drop (Uthaisangsuk 2008), and the fractography by scanning electron microscopy (SEM) (Min 2011). Among them, the inverse method of parameter identification gains the most popularity. The essence of the inverse identification approach is to seek for a best combination of all model parameters that is able to most accurately predict the mechanical properties of an experimental test.

In the general framework of the inverse approach, many optimization algorithms have been developed in the literature for effectively identifying the material parameters of a damage model. By the use of the neural network method, Abendroth (2003) successfully identified the damage parameters, plastic deformation and failure characteristics of ductile materials in a small punch test. The employed neural network consists of 101 input units, 25 hidden units and five output units, aiming to build up a database by matching the experimental and simulated force-displacement curves. The identified damage model was subsequently tested for three types of ductile steels (10MnMoNi55, 18Ch2MFA, StE-690). Springmann (2005) proposed a gradient-based nonlinear optimization algorithm, aiming to minimize the least-squares functional between the measured and simulated force-displacements data. Finite element (FE) simulations implemented with the identified model were then used for characterizing the damage property of a notched StE 690 cylinder subjected to a uniaxial tension. Abbasi (2012) applied the response surface methodology to derive the damage parameters of the GTN model for different monolithic blanks of tailor welded blanks. With the identified model parameters, the forming limit diagrams were subsequently investigated and reasonable agreements were achieved between experimental and simulation results. By comparing the experimental and simulated surface displacements of a metallic plate, Abbasi

(2013) also employed the method of artificial neural networks for identifying the GTN damage parameters. The numerical simulations implemented with the identified model were found in excellent agreement with experimental results for both hydroforming and Erichsen tests. By employing a hybrid particle swarm optimization and performing the uniaxial tensile test of smooth cylinders, Zhong (2016) determined the damage parameters of ductile steel 3Cr1MoV. The optimized parameters were subsequently utilized to investigate the relation between critical void fraction and stress triaxiality during the tensile test of notched specimens. Also by the response surface methodology, Wang (2017) determined the damage parameters of the GTN model for high-strength steel BR1500HS in the temperature range 20-800 °C. Temperature-dependent dynamic recrystallization and microvoid fraction evolution were subsequently explored on the basis of the identified model.

All literature works reviewed above reveal that, for any ductile metal, the application of the GTN damage model is composed of two steps. The first of which is the identification of all model parameters for the given material type. Only with appropriately identified parameters, the GTN damage model can be used for investigating the damage mechanics of the same material. Since in most cases the damage properties cannot be experimentally verified and validated, it is often hoped and assumed that the predictions by FE simulations implemented with the identified GTN model are reliable.

In this work, we first aim to extend the application of the GTN damage model to the Q345 steel (Chinese code), a typical microalloyed ductile steel that is extensively used in the manufacturing of mechanical and civil structures in China. In order to accurately characterize the microscopic damage properties of this material, it is therefore of great importance to correctly identify all GTN model parameters. In view of the large number of model parameters, it seems impractical to simultaneously identify all 13 GTN parameters. Consequently, we chose to first experimentally determine the four elastic and plastic parameters from the uniaxial tensile test of smooth Q345 cylinders. Being the most important damage properties, three void fraction ratios in the model are taken as the parameters to be identified from the force-displacement curves of notched Q345 steel cylinders. They correspond to the void volume fraction of void seeds, at coalescence and at the complete failure. As a well developed optimization algorithm, the response surface methodology is used for the identification (Abbasi 2012, Wang 2017). Finally, the numerical values for the remainder of the damage parameters and the three correction constants of the GTN model are uniquely determined from open literatures without identification. It is worth pointing out that although only the three void fractions are identified in the present study, other choices of identification parameters can be equally implemented without additional difficulties.

The second purpose of this work aims to the characterization of the void growth rate in the uniaxial tensile simulation of notched Q345 steel cylinders. Simulations were performed in ABAQUS/Explicit with the identified as well as predetermined GTN parameters. As the

fundamental function for describing the micromechanical evolution of plastic damage in ductile metals, the void growth rate is up to the macroscopic stress triaxiality and equivalent plastic strain (Zhang 1989). From such a perspective, the void growth rate serves as a mapping bridging the macroscopic mechanical properties and the microscopic damage status. Unfortunately, the void growth rate can only be simulated and there is no experimental means available for direct measurement.

As an alternative, experimental measurements on acoustic emissions (AE) have been extensively used (El-Thalji 2015, Qiu 2017, Chou 2015, Aggelis 2016, Rehman 2016, Nair 2010, Yu 2011, Diamanti 2010). The physical origin of AE refers to the rapid release of localized strain energy in the form of transient elastic waves (Holcomb 1993). Early studies with the AE method focused on correlating the plastic deformation in ductile metals with the resultant AE activities (James 1971, Holt 1980, Friesel 1984). The primary sources of AE activities are thus found to be associated with the plastic deformation and structural evolution of localized microscopic defects such as voids, inclusions, dislocations, grain boundaries and cracks. The AE monitoring therefore provides an indirect means for detecting the intrinsic damage evolution in ductile metals (Elfergani 2013, Aker 2014, Abdelrahman 2015, Gholizadeh 2015, Njuhovic 2015, Zou 2017, Chai 2018).

As a result, it is strongly desired to establish a functional relation between the simulated void growth rate and the experimentally measurable AE signals. In terms of such a connection, the robustness of the identified GTN model on the microscopic damage characterization of Q345 steels can be further verified and validated. To the best of our knowledge, no such efforts have been attempted in the open literature. The remainder of this paper is structured as follows. In Section 2, we present the overall organization of the combined experimental and FE study on the damage evolution in notched Q345 cylinders subjected to uniaxial tensile forces. Section 3 presents the major findings of the

combined study, including the identification algorithm of the damage parameters, the damage properties predicted by FE simulations implemented with the identified GTN model, experimental measurements on the AE energy, the validation of void growth rate against AE energy, and a morphologic analysis on the fracture surface of a notched Q345 specimen. Finally, in Section 4, a few observations and conclusions are drawn from the combined experimental and simulation study.

2. Materials and methods

Fig. 1 illustrates the flowchart of the combined experimental test and FE simulations on the damage evolution in a microalloyed steel cylinder under the application of uniaxial tensile stress. For this purpose, an appropriate microscopic damage model that is able to accurately predict the void growth rate of a ductile metal must be chosen first. To expand the applicability of the damage model, a few model parameters are typically allowed to vary within certain intervals while the remainder can be predetermined. In this work, those fitting parameters are calibrated by two means. First, they are numerically optimized by comparing the force-displacement curve predicted from FE simulations with that generated from an experimental test. The optimization process is facilitated by the response surface methodology (RSM). Second, the void growth rate predicted from the FE simulations is correlated with the accumulative AE resulting from an experimental test on the exactly same specimen and loading condition as used in the simulations. Provided that both means of calibration are satisfactory, the damage model can be safely used for specimens with more complicated geometries and subjected to complex stress states. Due to the complexity of the combined experimental and simulation approach, key modules of the flowchart are further explained in detail as follows.

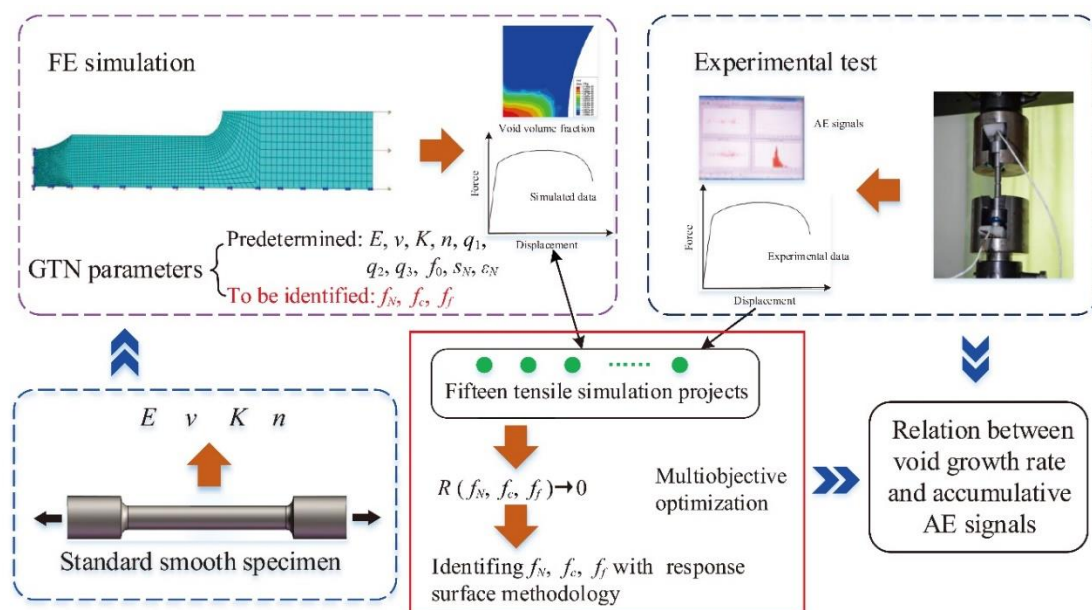


Fig. 1 Schematic diagram of the combined experimental test and FE simulations on the damage evolution in a microalloyed steel specimen

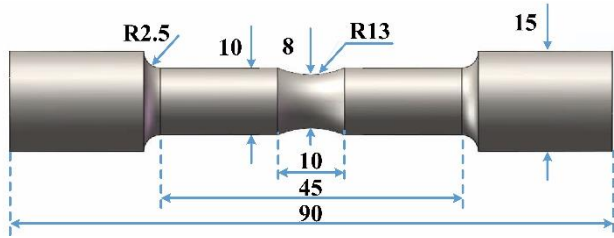


Fig. 2 Geometry of Q345 steel specimens that were used in the experimental test. All dimensions are in units of mm

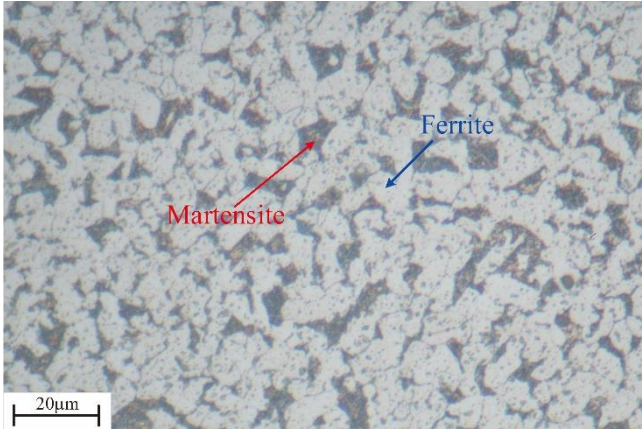


Fig. 3 The biphase microstructure of a typical Q345 steel. Ferrite and martensite sits are shown in light and dark gray, respectively.

Table 1 Mechanical properties and chemical compositions (wt.%) of Q345 steel

Material	Mechanical properties			Chemical compositions (wt.%)					
	σ_Y (MPa)	σ_U (MPa)	E (MPa)	C	Mn	Si	P	S	Ca
Q345 steel	408	533	200	0.17	1.42	0.31	0.020	0.031	0.10

2.1 Experimental setup

Fig. 2 shows the geometry of the specimens that were used in the tensile tests. Specimens were made from Q345 steel (Chinese Code), which is one of the primary materials for manufacturing ships, buildings, bridges and pressure vessels. The biphase microstructure of a typical Q345 steel is shown in Fig. 3, with ferrite in light and martensite in dark gray. Table 1 tabulates both the mechanical properties and chemical compositions. For easy monitoring of AE signals, specimens were manufactured into circular cylinders whose central segment was intentionally notched. Both ends of the specimens were finely polished in order to mount AE sensors.

The upper-right block of Fig. 1 shows the monitoring system for the AE energy that captures the microscopic damage evolution of an axially stretched specimen. Following the standard test methods for tension testing of metallic materials (ASTM E8/E8M), the uniaxial tensile test was conducted at the ambient temperature (300 K) by the use of an SANS universal testing machine. The relative stretching velocity between the two grips of the testing machine was set to 0.3 mm/min. The specimen and fixtures

were pinned together for avoiding vibration noises resulting from the possible relative slippage. Also, during the elastic stage a few loading and unloading cycles were implemented in order to fasten the connection between fixtures and the specimen. The standard resonant 55 kHz WD sensors with 40 dB preamplifiers were utilized to collect the AE signals. The AE sensors were firmly mounted on both ends of the notched specimen by using a thin film of vaseline. This way a good acoustic contact between the specimen and sensors can be guaranteed. A PCI-2 data acquisition board (Physical Acoustic Corporation, USA) was employed to record the AE signals generated during the tensile test. The signals were continuously recorded at the rate of 2 Mb/s. To filter out extraneous noises, a threshold level of 30 dB was set for all tests.

2.2 Damage characterization informed by acoustic emissions

During the tension test of Q345 steel specimens, AE signals are emitted because of the deterioration of structural integrity, including but not limited to the nucleation, growth and coalescence of voids and cracks. As a result, synergistic monitoring on the strength of AE signals provides a means of estimating the damage evolution of a loaded specimen (Tang 1990). The accumulative AE energy released due to the formation of a differential damage area dA can be written as

$$dE = n_r dA \quad (1)$$

where n_r stands for the AE energy per unit area. This quantity can be represented by the ratio between the accumulative AE energy (E_m) at failure and the corresponding cross-sectional area (A_0)

$$dE = \frac{E_m}{A_0} dA \quad (2)$$

Assuming that the strength of microdefects in a linearly elastic microelement follows Weibull distribution, the corresponding strain distribution takes the form

$$E(m) = \frac{m}{\varepsilon_0} \left(\frac{\varepsilon}{\varepsilon_0} \right)^{m-1} e^{-\left(\frac{\varepsilon}{\varepsilon_0} \right)^m} \quad (3)$$

where ε is the random variable (strain) of the Weibull distribution, ε_0 the scale parameter, and m the distribution uniformity. As a result, for the strain increment $d\varepsilon$ the cross-sectional area increases by

$$dA = A_0 E(\varepsilon) d\varepsilon \quad (4)$$

Combining equations (2) and (4) leads to

$$dE = E_m E(\varepsilon) d\varepsilon \quad (5)$$

Integrating the above equation gives the accumulative AE energy at a given strain level (ε)

$$E = E_m \int_0^\varepsilon E(x) dx \quad (6)$$

In the context of damage mechanics, a damage variable (D) is often defined to describe the overall damage status of a specimen. In view of equation (3), the damage variable at

the strain level ε can be represented by

$$D = \int_0^\varepsilon E(x) dx \quad (7)$$

A direct comparison between equations (6) and (7) reveals that the damage variable can be simply quantified as the ratio of the instantaneous accumulative AE energy with respect to the same quantity when the specimen is completely damaged

$$D = E/E_m \quad (8)$$

By the use of scanning electron microscope (SEM), Zhang *et al.* (1989) successfully observed the nucleation, growth and coalescence of microvoids. Based on extensive experimental studies and numerical simulations, they proposed a failure criterion for ductile metals

$$V_G = \bar{\varepsilon}_{pl} e^{1.5R_\sigma} \geq V_{GC} \quad (9)$$

where V_G represents the instantaneous void growth rate, $\bar{\varepsilon}_{pl}$ the equivalent plastic strain, R_σ the stress triaxiality, and V_{GC} the critical void growth rate at failure. The instantaneous void growth rate V_G serves as a material parameter for ductile metals, reflecting the instantaneous microscopic damage of a specimen. It is therefore reasonable to express the macroscopic damage variable D as

$$D = V_G/V_{GC} \quad (10)$$

Comparing equation (10) with (8), it is possible to make a connection between the instantaneous void growth rate and the accumulative AE energy, provided that their values at failure are given.

2.3 FE simulation of void growth

2.3.1 Meshing scheme and boundary conditions

FE simulations were also performed on the tensile test of notched Q345 cylinders as shown in Fig. 2. The simulations were implemented in ABAQUS/Explicit software package. Benefitting from the geometric symmetry, only a quarter of the Q345 steel specimen needs to be modeled. Proper constraints were introduced to remove those undesired displacement components perpendicular to the symmetry axes. The four-node axisymmetric reduced integration elements (CAX4R) were used to mesh the geometry, as shown in the upper-left block of Fig. 1. Given the large stress and strain gradient in the vicinity of the notched portion, this region is meshed with elements of size 0.1 mm. This size is close to the characteristic scale of the microstructural details of ductile steel, e.g. grain size and void spacing. For regions far away from the notch, coarser meshes were used. The size of the meshes was evenly ramped in between the notched cross-section and both ends. Due to the quasistatic nature of the tensile experiment, small temporal increments in FE simulations are required, resulting in a heavy demand on computational resources. To make a balance between the computational accuracy and efficiency, the mass scaling technique was employed in this work.

2.3.2 Microscopic damage model

In order to characterize the void growth rate in FE simulations, a yield criterion that is able to capture the temporal evolution of void volume fraction must first be established. The classical yield criteria, e.g. the maximum shear stress and the maximum distortion energy laws, cannot afford the evolution of microstructural damages such as voids and cracks. To fix the issue, Gurson proposed a new yield criterion to explicitly take the effect of void fraction evolution into account (Gurson 1977). Later, this criterion was further extended by Tvergaard and Needleman (1984) for further describing the nucleation, growth and coalescence of spherical voids in ideal plastic materials. In the literature, this model is conventionally referred to as the GTN damage model. The yielding surface of the GTN model is given by the function

$$\Phi = \left(\frac{\sigma}{\sigma_y}\right)^2 + 2q_1 f^* \cosh\left(\frac{3}{2} q_2 \frac{\sigma_h}{\sigma_y}\right) - (1 + q_3 (f^*)^2) = 0 \quad (11)$$

where $\sigma = \sqrt{3S_{ij}S_{ij}/2}$ is the macroscopic von Mises equivalent stress, $S_{ij} = \sigma_{ij} - \sigma_{ij}\delta_{ij}/3$ the deviatoric stress tensor, $\sigma_h = \sigma_{kk}/3$ the hydrostatic stress, σ_y the yield stress of the matrix material, and δ_{ij} the Kronecker delta. In addition to the yield stress σ_y , three fitting parameters, i.e. q_1 , q_2 and $q_3 = q_1^2$, are introduced to accommodate the differences among ductile metals. Most importantly, the GTN damage model takes into account the accelerating effects of void coalescence on void fraction ratio. The void volume fraction in the original Gurson's model was modified to

$$f^*(f) = \begin{cases} f & f \leq f_c \\ f_c + \kappa(f - f_c) & f > f_c \end{cases} \quad (12)$$

where κ represents the acceleration factor of void growth beyond coalescence

$$\kappa = \frac{1/q_1 - f_c}{f_f - f_c} \quad (13)$$

In equations (12) and (13), f_c and f_f are the critical volume fractions at void coalescence and at complete failure, respectively. The acceleration factor κ was introduced to characterize both the acceleration in void growth rate and the possible brittle fracture resulting from accumulative ductile damage.

During a loading process, the void volume fraction f increases due to both the growth of existing voids and the initiation of new voids. As a result, the total growth rate of void volume fraction can be written as

$$\dot{f} = \dot{f}_g + \dot{f}_n \quad (14)$$

In view of the incompressibility of the matrix during plastic deformation, conservation of mass leads to

$$\dot{f}_g = (1 - f) \dot{\varepsilon}_{pl}^{kk} \quad (15)$$

where $\dot{\varepsilon}_{pl}^{kk}$ represents the volumetric part of the plastic strain. The nucleation rate of new voids follows the strain-controlled relation

$$\dot{f}_n = \frac{f_N \bar{\epsilon}_{pl}}{s_N \sqrt{2\pi}} e^{-\frac{1}{2} \left(\frac{\bar{\epsilon}_{pl} - \epsilon_N}{s_N} \right)^2} \quad (16)$$

where $\bar{\epsilon}_{pl}$ denotes the equivalent plastic strain and f_N is the volume fraction of void seeds, i.e. those particles that are available for nucleating voids. Note that the statistical Gaussian distribution is assumed for the nucleation of new voids, with the mean equivalent plastic strain ϵ_N and the standard deviation s_N .

2.3.3 Identification of the GTN damage model

To implement the GTN damage model in FE simulations, we require all model parameters. They include the four elastic-plastic properties of Q345 steel (E , ν , K , n), the three model correction factors (q_1 , q_2 , q_3), and the six damage parameters (f_0 , f_N , f_c , f_f , s_N , ϵ_N). Among these model parameters, E , ν , K , n , f_0 denote Young's modulus, Poisson's ratio, the strength coefficient, the strain-hardening exponent, and the initial value of void volume fraction prior to loading, respectively. All the other parameters have been explained in the previous subsection.

The four elastic-plastic properties in the first group can be easily determined by performing uniaxial tensile tests of standard smooth specimens (without notching). Under the application of a monotonic loading, steel specimens exhibit strain-hardening behavior beyond initial yielding. In literature studies, a Hollomon-type hardening rule is extensively used for describing such a behavior

$$\sigma_p = K \epsilon_n^p \quad (17)$$

Fig. 4 shows the true stress and true plastic strain curve recorded in the tensile test of a typical smooth Q345 steel cylinder. The experimental data was numerically fitted by equation (17), resulting in both hardening parameters (Table 2). The Young's modulus and Poisson's ratio were extracted from the linear stage of the uniaxial tension test, as shown in Table 2.

Informed by the chemical composition and metallographical structure of steel, Franklin (1969) proposed a quantitative assessment formula for estimating the initial void volume fraction in pristine steels

$$f_0 \approx 0.054 \left(wt_S(\%) - \frac{0.001}{wt_{Mn}(\%)} \right) \quad (18)$$

Referring to the weight percentages of steel and manganese of Q345 steel as given in Table 1, the initial void fraction can be easily determined from the above equation (Table 2).

For the three model correction factors and the remainder of the damage parameters, the choice on those that need to be identified from experimental tests is not unique (Benseddiq and Imad 2008, Oral *et al.* 2012, Kiran and Khandelwal 2014). In this work, we chose to investigate the robustness of the GTN damage model on Q345 steel by identifying three volume fractions, namely the void fraction of void seeds f_N , at coalescence f_c and at complete failure f_f . They are allowed to vary within certain intervals that were carefully determined from their available literature values (Table 2). The others were predetermined by referring to Kiran and Khandelwal (2014), as tabulated in Table 2.

To determine the temporal evolution of void volume fraction, the three fitting parameters of the GTN damage model must first be identified against experimental data. Among available techniques, the RSM method is an effective approach for simultaneously exploring the interactions among multiple independent variables and multiple responses. This method has found wide applications in the field of mathematics and statistics. The central idea is to search for optimum responses by implementing a series of trial combinations of independent variables (Myers *et al.* 2012).

To be specific, we are interested in optimizing the three damage parameters (independent variables) of the GTN model in order to get the most accurate predictions from the FE simulations. Care must be practiced on the selection of response functions. Since the microscopic damage evolution can only be indirectly validated by the accumulative AE energy, the damage variable itself is not a suitable candidate to response functions. In the uniaxial tensile test of Q345 cylinders, the force-displacement curve is often the easiest available data (Fig. 5). We therefore decided to focus on both the axial forces and displacements at the ultimate strength and at the final failure, because the

Table 2 Predetermined values and proposed intervals for GTN damage model parameters that were used in the uniaxial FE simulations of notched Q345 steel cylinders

Parameters		Description	Value
Elastic-plastic	E	Young's modulus (MPa)	190000
	ν	Poisson's ratio	0.3
	K	Strength coefficient (MPa)	953.27
	n	Strain-hardening exponent	0.2015
Model correction	q_1	Void interaction factor	1.5
	q_2	Void interaction factor	1.0
	q_3	Void interaction factor	2.25
Damage	f_0	Initial void volume fraction	0.0016
	f_N	Void fraction of void seeds	To be fitted (0.01~0.07)
	f_c	Void fraction at coalescence	To be fitted (0.01~0.20)
	f_f	Void fraction at failure	To be fitted (0.20~0.45)
	s_N	Standard deviation	0.1
	ϵ_N	Mean effective plastic strain	0.3

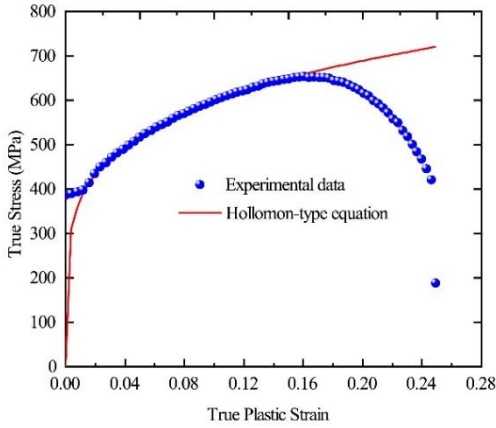


Fig. 4 Experimental (blue spheres) and numerically fitted (red solid) true stress and true plastic strain curves

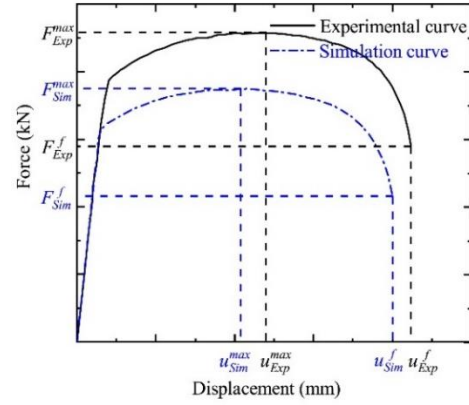


Fig. 5 Schematic diagram illustrating the construction of four response functions that are used for identifying the three GTN model parameters (f_N , f_c and f_f)

GTN damage model was originally designed to model the plastic failure of ductile metals. As shown in Fig. 5, the differences of the ultimate and failure forces/displacements between the experimental and simulation curves were chosen as the response functions

$$R_1 = u_{Exp}^{max} - u_{Sim}^{max} \quad (19a)$$

$$R_2 = F_{Exp}^{max} - F_{Sim}^{max} \quad (19b)$$

$$R_3 = u_{Exp}^f - u_{Sim}^f \quad (19c)$$

$$R_4 = F_{Exp}^f - F_{Sim}^f \quad (19d)$$

As has been mentioned above, our first goal is to identify the three independent variables (f_N , f_c and f_f) by minimizing the four responses (R_1 , R_2 , R_3 and R_4). Both the optimization algorithm and the identified parameters are detailed in the next section.

3. Results and discussion

FE simulations implemented with the GTN damage model are able to directly reveal the damage evolution in ductile metals to a certain extent. In contrast, in experimental tests the AE energy can only indirectly reflect the void activities of ductile specimens under the application of external loads. From this perspective, FE simulations are often preferred to experimental tests for predicting the evolution of void growth rate. Nonetheless, for a given ductile metal, all parameters of the GTN damage model must be predetermined prior to performing simulation runs (Table 2). In this section, we first present the identifying algorithm and results for the three damage parameters (f_N , f_c and f_f), followed by a detailed FE analysis on the damage evolution of notched Q345 steel cylinders with the optimized model parameters. The FE results on damage evolution are subsequently correlated with the experimental AE energy in order to verify the accuracy and robustness of the FE approach.

Table 3 Fifteen combinations of the three independent variables generated by the BBD method and the corresponding responses predicted from FE simulations implemented with the GTN damage model

Run	f_N	f_c	f_f	Responses			
				R_1	R_2	R_3	R_4
1	0.010	0.010	0.325	0.069701	211.10	0.080254	265.10
2	0.070	0.010	0.325	-0.060204	-130.30	-0.224370	2202.30
3	0.010	0.200	0.325	0.054740	193.90	0.282729	-2718.70
4	0.070	0.200	0.325	-0.030204	-107.90	-0.080203	351.40
5	0.010	0.105	0.200	0.069740	213.60	0.160229	-333.10
6	0.070	0.105	0.200	-0.060204	-130.30	-0.224370	2202.30
7	0.010	0.105	0.450	-0.030201	-108.10	-0.100200	948.70
8	0.070	0.105	0.450	0.084740	214.60	0.306929	-2776.70
9	0.040	0.010	0.200	-0.030204	-107.90	-0.100203	948.80
10	0.040	0.200	0.200	-0.014962	21.00	-0.206627	2614.20
11	0.040	0.010	0.450	0.000035	24.70	0.020033	-98.10
12	0.040	0.200	0.450	0.000035	23.20	-0.079965	1097.50
13	0.040	0.105	0.325	0.000035	24.70	0.040033	-1024.90
14	0.040	0.105	0.325	-0.004971	29.80	0.024042	-101.80
15	0.040	0.105	0.325	0.002030	24.70	0.009034	-96.80

$$R_1 = 0.09985 - 3.36f_N + 0.23f_c - 0.0826f_f + 3.94f_Nf_c - 1.0002f_Nf_f - 0.32f_cf_f + 18.54f_N^2 - 1.168f_c^2 + 0.29f_f^2 \quad (21a)$$

$$R_2 = 301.1 - 7605.64f_N + 83.89f_c - 114.75f_f + 3473.68f_Nf_c - 53.33f_Nf_f - 46.32f_cf_f + 23675.93f_N^2 - 924.28f_c^2 + 192.53f_f^2 \quad (21b)$$

$$R_3 = -0.245 - 6.92f_N + 3.39f_c + 1.51f_f - 5.1f_Nf_c - 9.78f_Nf_f - 2.25f_cf_f + 63.45f_N^2 - 7.34f_c^2 - 0.9f_f^2 \quad (21c)$$

$$R_4 = 5438.98 + 15193.1f_N - 33199.67f_c - 21344.55f_f + 99377.19f_Nf_c + 1.629 \times 10^5 f_Nf_f + 12418.95f_cf_f - 4.61 \times 10^5 f_N^2 + 59359.65f_c^2 + 13287.73f_f^2 \quad (21d)$$

3.1 Identification of damage parameters

Within the context of RSM, the Box-Behnken Design (BBD) method is often employed for preparing repeated experiments or simulation runs (Myers *et al.* 2012, Montgomery 2013). The BBD method can be summarized in terms of the mathematical formula

$$R = A_0 + \sum_{i=1}^n A_i X_i + \sum_{i=1}^n \sum_{j=i}^n A_{ij} X_i X_j \quad (20)$$

where R is the predicted response, A_0 the intercept term, A_i the linear coefficient to the i th variable, A_{ij} the interaction between the i th and j th variables, and n the total number of independent variables. Following the BBD method, each of the three independent variables needs to be evaluated at three specific levels. For the present study, the three variables are selected at three evenly spaced levels, i.e. $f_N = 0.01, 0.04, 0.07$, $f_c = 0.01, 0.105, 0.20$ and $f_f = 0.20, 0.325, 0.45$, indicating the low, intermediate and high level (Table 2). On the basis of all possible combinations of independent variables, the BBD method requires at least fifteen simulation projects for the purpose of parameter identification. It is worth pointing out that these fifteen combinations are unique, as tabulated in Table 3. It is also noted that the last three rows of Table 3 contain three identical combinations of the three independent variables. This choice is also due to the requirement by the BBD method and aims to accommodate the uncertainty of simulation/experimental results, since even for the identical combinations of independent variables FE simulations may result in quite different responses.

For each specific combination of the three independent variables, the parameters of the GTN damage model are now complete and FE simulations can be performed to find the four responses. The four response functions as defined in equations (19a-d) for all fifteen combinations of the independent variables are also tabulated in Table 3. Substituting the data in Table 3 back into equation (20) and performing the RSM analysis (Myers *et al.* 2012) lead to the explicit forms of the four response functions in terms of the three independent variables.

The accuracy of the developed response functions (21a-d) was first verified for examining the reliability of the RSM method. Figs. 6a-d aim to check the consistency

between the true and predicted response functions. In all four subfigures, the straight lines indicate the best fitted targets along which the predicted responses are identical to the corresponding true values. It is seen that in Figs. 6a-d all data points appear quite close to the diagonals, indicating high correlations between the true and predicted response functions.

Prior to solving the simultaneous equations (21a-d) for the optimal independent variables, multifunction regression analysis was conducted to test the influence of independent variables on responses. In the regression analysis, the analysis of variance was systematically performed to evaluate the statistical significances of individual independent variables as well as their interactions. The results of the variance analysis are tabulated in Table 4. The table is divided into four blocks with each one corresponding to one of the four response functions.

Both the F -value and p -value are important indicators for measuring the significance level (Montgomery 2013). A large F -value or a small p -value represents high significance level of the variable/interaction on response functions. Moreover, the lack of fit (LF) index is a measure to the probability of disagreement between the true and predicted responses. The absolute difference between them is represented by the residual error (RE) index, indicating the accuracy of the prediction model. For both the LF and RE index, small values are desired. In addition, for all four response functions both the determination coefficients (R^2) and the adjusted determination coefficients (R_{adj}^2) are very close to unity, also suggesting the wellness of the prediction model. In summary, results of the analysis of variance confirm the accuracy of the prediction model. As a result, equations (21a-d) are reliable for correlating the three damage parameters (f_N , f_c and f_f) of the GTN model with the four response functions (R_1 , R_2 , R_3 and R_4).

Given equations (21a-d), the parameter identification process is now transformed into a multiobjective optimization problem. Recall that the response functions (19a-d) were defined as the differences between the maximum and failure forces/displacements resulting from the experimental tests and FE simulations. Therefore, the ideal solutions of the three identification parameters should result in four response functions that all are very close to zero. A simple least squares analysis on equations (21a-d) leads to the optimal numerical values of the three void volume fractions: $f_N = 0.045$, $f_c = 0.126$ and $f_f = 0.26$.

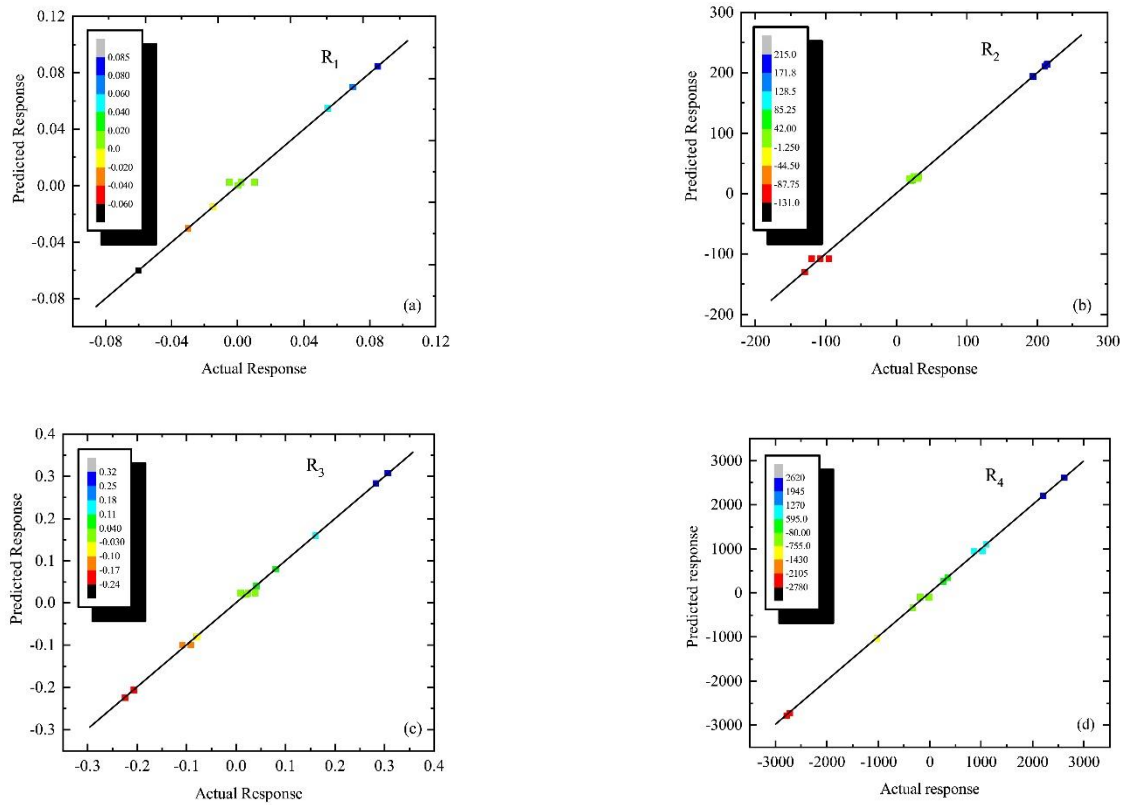


Fig. 6 Verification and validation of the identification model (21a-d) for all four response functions

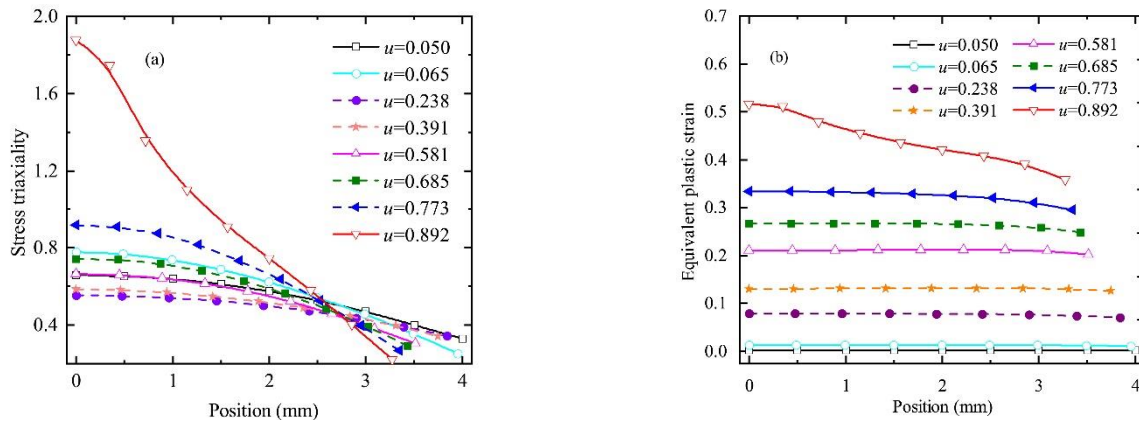


Fig. 7 Variations of (a) stress triaxiality and (b) equivalent plastic strain along the radial direction on the notched cross-section of the Q345 steel cylinder

3.2 FE simulations with the identified GTN model

With the three void volume fractions (f_N , f_c and f_p) of the GTN damage model successfully identified in the previous subsection, quasi-static uniaxial FE simulations were performed on a notched Q345 steel cylinder. Results of the FE simulations show that the uniaxial stress reaches the ultimate strength (687.58 MPa) at the axial displacement 0.650 mm. The corresponding axial strain reads 0.129. The notched specimen completely fails at the axial displacement 0.892 mm. The corresponding axial

stress and strain are 366.04 MPa and 0.246, respectively. The numerical values of these important elastic-plastic indices are found to be in excellent agreement with those produced by experimental tests.

Figs. 7a and b show variations of the stress triaxiality and the equivalent plastic strain along the radial direction on the notched cross-section. It can be seen that at all eight loading levels, the maximum stress triaxiality always occurs at the center (Fig. 7a). The stress triaxiality decreases monotonically as the radial coordinate changes from the center to the perimeter of the cross-section. Moreover, the rate of decay increases with the magnitude of the axial

Table 4 Results of the analysis of variance on the prediction model (21a-d)

Source	df	SS ¹	F-value	p-Value	df	SS ¹	F-value	p-Value	
		<i>R</i> ₁				<i>R</i> ₂			
Model	9	0.026	125.78	< 0.0001	9	2.096×10 ⁵	4402.29	< 0.0001	
<i>f</i> _N	1	0.023	1023.32	< 0.0001	1	2.072×10 ⁵	39153.62	< 0.0001	
<i>f</i> _c	1	1.128×10 ⁻⁴	5.00	0.0756	1	13.52	2.56	0.1708	
<i>f</i> _f	1	1.125×10 ⁻⁴	4.99	0.0759	1	1.45	0.27	0.6236	
<i>f</i> _N <i>f</i> _c	1	5.054×10 ⁻⁴	22.40	0.0052	1	392.04	74.09	0.0003	
<i>f</i> _N <i>f</i> _f	1	5.627×10 ⁻⁵	2.49	0.1751	1	0.16	0.030	0.8688	
<i>f</i> _c <i>f</i> _f	1	5.623×10 ⁻⁵	2.49	0.1752	1	1.21	0.23	0.6527	
<i>f</i> _N ²	1	1.028×10 ⁻³	45.58	0.0011	1	1676.47	316.83	< 0.0001	
<i>f</i> _c ²	1	4.106×10 ⁻⁴	18.20	0.0080	1	256.92	48.56	0.0009	
<i>f</i> _f ²	1	7.363×10 ⁻⁵	3.26	0.1306	1	33.42	6.32	0.0536	
LF ²	3	3.825×10 ⁻¹⁰	2.261×10 ⁻⁶	1.0000	3	0.25	6.36×10 ⁻³	0.9991	
RE ³	5	1.128×10 ⁻⁴			5	26.46			
	<i>R</i> ²	0.9956	<i>R</i> _{adj} ²	0.9877	<i>R</i> ²	0.9999	<i>R</i> _{adj} ²	0.9996	
		<i>R</i> ₃				<i>R</i> ₄			
Model	9	0.33	440.66	< 0.0001	9	3.109×10 ⁷	2.419×10 ⁵	< 0.0001	
<i>f</i> _N	1	0.22	2646.00	< 0.0001	1	1.254×10 ⁷	8.778×10 ⁵	< 0.0001	
<i>f</i> _c	1	0.060	713.50	< 0.0001	1	1.169×10 ⁷	8.184×10 ⁵	< 0.0001	
<i>f</i> _f	1	0.011	127.75	< 0.0001	1	2.985×10 ⁶	2.090×10 ⁵	< 0.0001	
<i>f</i> _N <i>f</i> _c	1	8.500×10 ⁻⁴	10.09	0.0246	1	3.209×10 ⁵	22467.48	< 0.0001	
<i>f</i> _N <i>f</i> _f	1	5.380×10 ⁻³	63.89	0.0005	1	1.493×10 ⁶	1.045×10 ⁵	< 0.0001	
<i>f</i> _c <i>f</i> _f	1	2.844×10 ⁻³	33.78	0.0021	1	86995.50	6091.55	< 0.0001	
<i>f</i> _N ²	1	0.012	143.00	< 0.0001	1	6.345×10 ⁵	44426.22	< 0.0001	
<i>f</i> _c ²	1	0.016	192.23	< 0.0001	1	1.060×10 ⁶	74200.39	< 0.0001	
<i>f</i> _f ²	1	7.368×10 ⁻⁴	8.75	0.0316	1	1.592×10 ⁵	11144.77	< 0.0001	
LF ²	3	1.883×10 ⁻¹⁰	2.981×10 ⁷	1.0000	3	0.000	0.000	1.0000	
RE ³	5	4.210×10 ⁻⁴			5	71.41			
	<i>R</i> ²	0.9987	<i>R</i> _{adj} ²	0.9965	<i>R</i> ²	0.9996	<i>R</i> _{adj} ²	0.9897	

¹SS: Sum of squares; ²LF: Lack of fit; ³RE: Residual error

tension. All stress triaxiality curves intersect in the vicinity of the radial coordinate $R \approx 2.6$ mm. For $R < 2.6$ mm, the stress triaxiality increases during the loading process. The opposite is true for regions with $R > 2.6$ mm. On the other hand, the variation of the equivalent plastic strain shows somewhat different behavior from that of the stress triaxiality (Fig. 7b). Under the application of relatively small axial forces, the equivalent plastic strain remains a constant throughout the notched cross-section. At elevated axial loadings, the equivalent plastic strain becomes a decreasing function of the radial coordinate. No intersections among the eight equivalent plastic strain curves were found, revealing that throughout the notched cross-section the equivalent plastic strain increases with the applied axial force. Based on Figs. 7a and b, it can be concluded that the central region of the notched cross-section is most susceptible to plastic deformations and should be examined in more detail.

Figs. 8a-h show eight snapshots on the temporal evolution of the void volume fraction in the vicinity of the notch during the uniaxial tensile simulation. Each snapshot corresponds to one of the loading levels as studied in both Figs. 7a and b. Consistent with what have been found for the stress triaxiality and the equivalent plastic strain, for all

loading levels the maximum void fraction always occurs at the center of the narrowest cross-section. As the axial loading increases, voids expand rapidly away from the central region of the notch, indicating the ductile failure mechanism of the Q345 steel cylinder. In Fig. 8h, the maximum void fraction, found again at the center of the notch, reaches the critical value ($f_j = 0.26$) and results in the fracture of the Q345 cylinder along the notched cross-section.

3.3 Accumulative AE energy

Experimental studies show that the temporal evolution of AE signals is a valid descriptor for characterizing the microscopic damage process of a ductile metal specimen. As a result, it is desired to establish a connection between the void growth rate predicted from FE simulations and experimentally detected AE signals. In this subsection, we first present the temporal evolution of AE signals detected during the uniaxial tensile test of a notched Q345 steel cylinder. The experimental data was subsequently used for verifying and validating the void growth rate determined from FE simulations of the exactly same specimen.

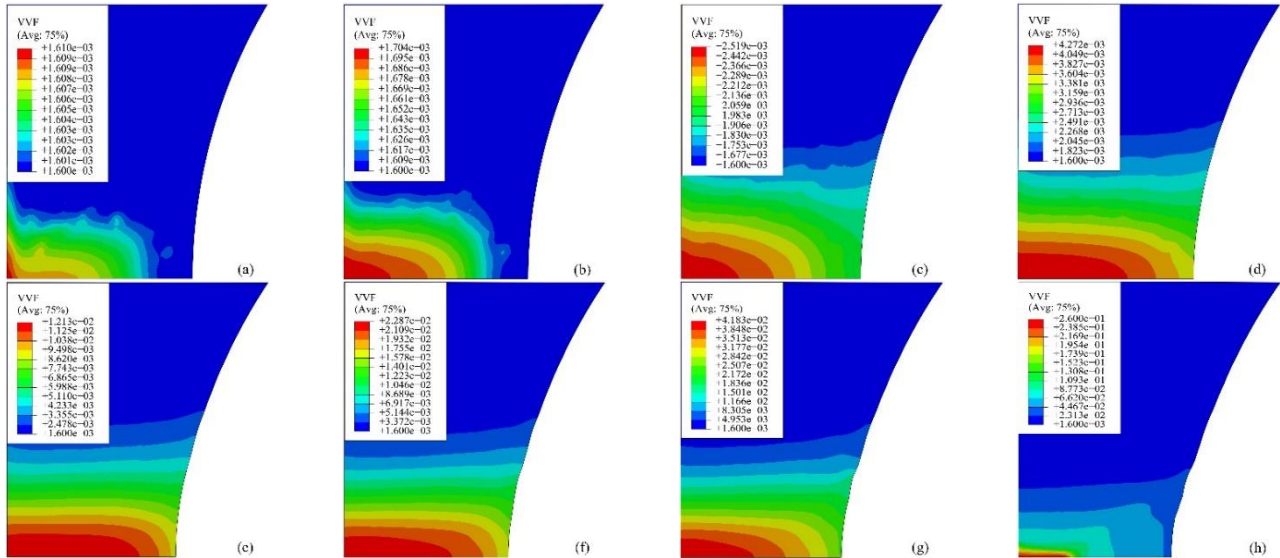


Fig. 8 Distribution of the void volume fraction (VVF) in the vicinity of the notch at eight loading levels as given in Figs. 7a and b

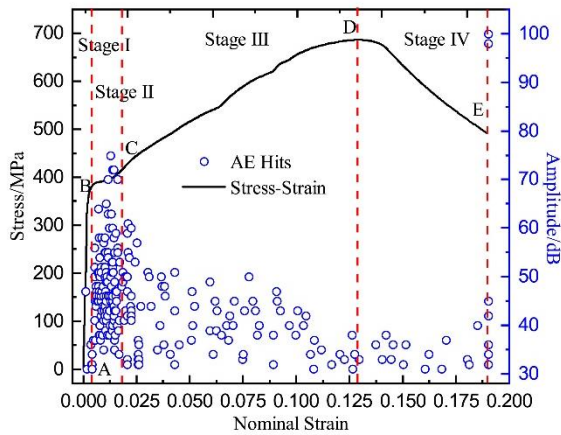


Fig. 9 The evolution of nominal stress and AE signals during the uniaxial tension test of a notched Q345 steel cylinder

Fig. 9 shows simultaneously the stress-strain curve and the AE signals produced by the uniaxial tensile test of a Q345 steel cylinder. The whole damage process up to fracture can be divided into four stages bounded by five points (A, B, C, D, E) on the stress-strain curve. The first stage corresponds to the elastic deformation of the tensioned cylinder. It is seen that, although the macroscopic deformation behaves elastic, AE signals with low amplitude are detected. This phenomenon can be explained by the local yielding of the inhomogeneously distributed microstructures (Moorthy *et al.* 1995, Han *et al.* 2011), since the yield strength of these microstructures is lower than that of the bulk steel. Due to the limited amount of microstructures in pristine steel specimens, in this stage the local yieldings are not reflected on the stress-strain curve. The second stage of the stress-strain curve represents the initial yielding of the Q345 cylinder. Enormous AE signals were detected, due to the initiation and propagation of

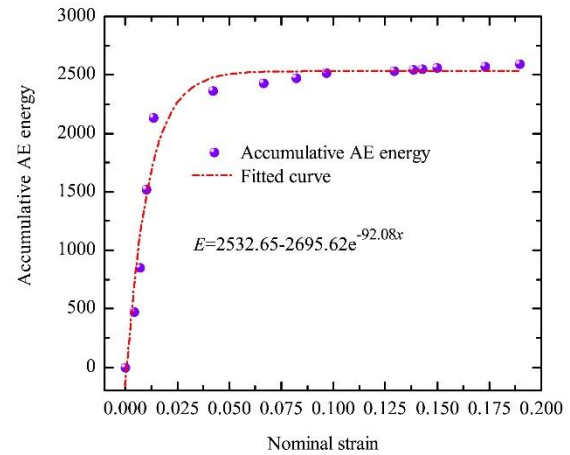


Fig. 10 The evolution of accumulative AE energy with the nominal strain during the uniaxial tensile test of the notched specimen

dislocations. It is seen that the amplitude of some AE signals is higher than 70 dB. The third stage reflects the strain hardening behavior of the ductile specimen, accompanied by less AE events than those found in the initial yielding stage. Also, the amplitude of all AE signals is lower than 65 dB. The mobility of dislocations is now partially suppressed due to the coalesce and tangling of propagating dislocations. The strain softening or further necking of the notched specimen is represented by the last stage of the stress-strain curve. Tremendous AE signals are detected and the amplitude reaches as high as 100 dB when the notched cylinder fractured. These results are found to be consistent with existing studies (Han *et al.* 2011, Mukhopadhyay *et al.* 2007, Kumar *et al.* 2012).

Fig. 10 shows the evolution of accumulative AE energy as a function of the uniaxial nominal strain detected during the tension test of the notched Q345 specimen. It should be noted that the AE signals induced by the final fracture of the

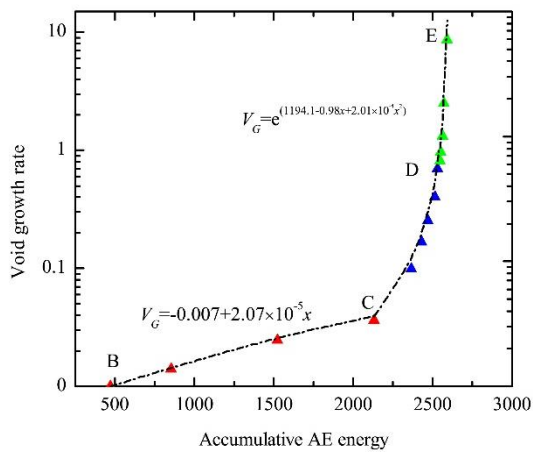


Fig. 11 Correlation between void growth rate and accumulative AE energy for the notched specimen

specimen have been intentionally eliminated in order to avoid the outburst of the curve. As can be observed from the figure, the accumulative AE energy increases dramatically with the strain up to the beginning of the hardening stage, owing to the local yielding of microstructures. During the hardening and softening stages, the rate of increase of the accumulative AE energy gradually slows down, reflecting the suppressed dislocation activity. The variation of the overall accumulative energy is well fitted by an exponential function, as given in the figure. This trend is consistent with the theoretical model of the instantaneous accumulative AE energy given in Section 2.2.

3.4 Validation of void growth rate against acoustic emissions

In this subsection, we aim to verify and validate the microscopic damage evolution of the notched Q345 specimen against the experimental accumulative AE energies. Given the particular geometry of the Q345 specimens, the eventual failure is expected to occur along the notched cross-section of all specimens. As a result, the notched cross-section can be taken as a reference during the micromechanical characterization of the damage evolution. The instantaneous void growth rate of the reference point is then calculated from equation (9) for the five critical stress levels on the stress-strain curve (Fig. 9). A direct comparison between the instantaneous void growth rate and the accumulative AE energy is made in Fig. 11. The data during the elastic deformation (stage I) was not shown in the figure, because of the low level of damage activity. During initial yielding (stage II), the instantaneous void growth rate is found to be in linear proportionality with the accumulative AE energy. It is noted that the ordinate of the figure is expressed in terms of the linear logarithm scale. As explained in the previous subsection, the rapid evolution of the accumulative AE energy is due to the active emissions of transient elastic waves. The void growth rate evolves linearly with the accumulative AE energy, with its maximum value being less than 0.05. This rate of increase

is consistent with the nucleation and propagation of dislocations during the yielding stage.

During the strain hardening and softening (stage III and IV), the instantaneous void growth rate increases exponentially with the accumulative AE energy. As reflected by Fig. 10, during the last two stages of the tension test, the evolution of the accumulative AE energy behaves quite stable. However, the void growth rate evolves rapidly from approximately 0.036 to 8.604. The trend of transition of the void growth rate as a function of the accumulative AE energy characterizes the damage evolution of the notched specimen. Following the standard reasoning, it is believed that these mathematical formulas can be used for predicting the equivalent damage status of Q345 specimens with more complex geometries and loading conditions.

3.5 Morphologic fracture analysis

When a ductile specimen is subjected to external loading, void typically initiates around non-metallic inclusions and second-phase particles. These events can be viewed as the onset of ductile fracture. The morphology of the fracture surface of the tested specimen was examined by the scanning electron microscope (SEM) for investigating the failure mechanism (Fig. 12). At the microscale, large dimples were found at the central region of the fracture surface whereas shear lips form near the perimeter. The area fraction of the shear lip zone is an important index for indicating the presence of necking and the ductile failure mechanism of the notched steel cylinder. The area of the shear lip zone approaches less than a half of the total cross-sectional area of the specimen, manifesting the obvious necking stage during the uniaxial test. The fracture pattern is decided by the stress state in the specimen. As indicated in Fig. 7, the maximum stress triaxiality occurs at the center of the notched cross-section and gradually decays along the radius. As a result, the stress state changes from triaxial to biaxial tension, resulting in the shear failure near the perimeter of the notched cross-section. Macroscopically, the fracture surface conforms to the typical cup-cone morphology. Moreover, voids are found to coalesce at the center of the notched cross-section. It is evident that the continuous growth and coalescence of voids dictate the plastic deformation of the specimen and reduce the loading capacity until complete failure. The heterogeneous inclusions in the matrix are brittle in nature and behave indeed brittle under the application of external loads. The void activities originated from dislocation dynamics and fractures of heterogeneous inclusions serve as the main sources of AE energy (Horváth *et al.* 2016).

4. Conclusions

We performed a combined experimental and finite element (FE) study on the microscopic damage evolution in Q345 steel specimens. In the FE simulations, the volume fraction of void seeds ($f_N=0.045$), at coalescence ($f_c=0.126$) and at complete failure ($f_f=0.26$) of the GTN damage model were successfully identified against the

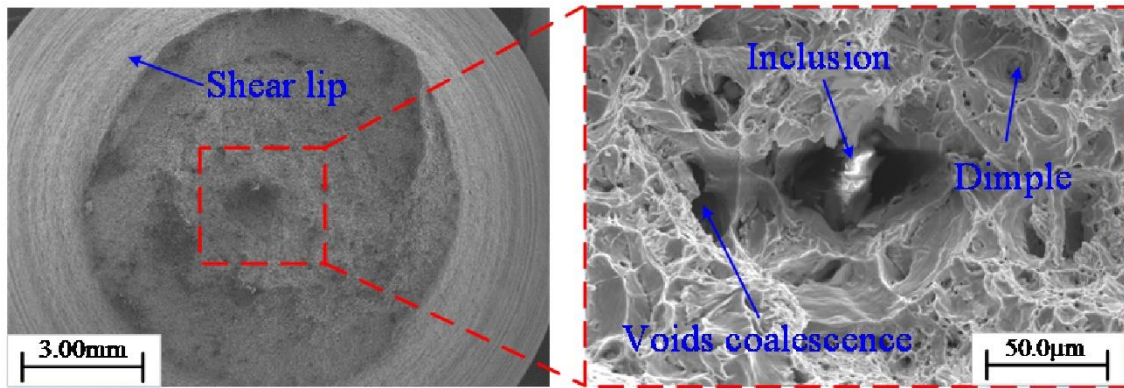


Fig. 12 SEM image of the fracture surface resulting from the uniaxial tensile test of the notched steel cylinder

uniaxial tensile test of Q345 cylinders. The void growth rate is subsequently simulated by the identified GTN model and also correlated with the acoustic emissions (AE) extracted from experimental monitoring of tensioned Q345 cylinders. Several observations and conclusions can be drawn from the combined analysis.

- FE results demonstrate that, during the uniaxial tensile simulations of Q345 cylinders, the stress triaxiality, equivalent plastic strain and void volume fraction all increase with the uniaxial strain of the notched specimen. Moreover, under any strain state the maximum value of these plastic indices always appears at the center of the notched cross-section.

- Massive AE energies were detected during the microyielding and yielding stages of the uniaxial stress-strain curve. The accumulative AE evolves exponentially throughout the tensile test.

- A correlation between the void growth rate predicted by the FE simulations and the accumulative AE was mathematically performed. In the first two stages of the force-displacement curve, the void growth rate is found to grow linearly with the accumulative AE. Extensive void growth and coalescence were identified during the strain-hardening and softening stages, indicated by the exponential variation of the void growth rate with the AE.

- The typical cup-cone morphology of the fracture surface of the tensioned Q345 cylinder specimen indicates that the heterogeneous inclusions serve as the primary sources for void nucleation. The ductile fracture of the notched specimen is resulting from the successive evolution of void activities, including void nucleation, growth and coalescence.

Acknowledgments

This work was supported by the National Natural Science Foundation of China [grant number 11872149], the Natural Science Foundation of Jiangsu Province [grant number BK20161411], the National Key Research and Development Program [grant number 2017YFC0702800], the Fundamental Research Funds for the Central Universities, and the Postgraduate Research Practice Innovation Program of Jiangsu Province [grant number KYCX17-0052].

References

- Abbasi, M., Bagheri, B., Ketabchi, M. and Haghshenas, D. (2012), "Application of response surface methodology to drive GTN model parameters and determine the FLD of tailor welded blank", *Comput. Mater. Sci.*, **53**(1), 368-376. <https://doi.org/10.1016/j.commatsci.2011.08.020>.
- Abbassi, F., Belhadj, T., Mistou, S. and Zghal, A. (2013), "Parameter identification of a mechanical ductile damage using Artificial Neural Networks in sheet metal forming", *Mater. Design*, **45**, 605-615. <https://doi.org/10.1016/j.matdes.2012.09.032>.
- Abdelrahman, M., ElBatanouny, M.K., Ziehl, P., Fasl, J., Larosche, C.J. and Fraczek, J. (2015), "Classification of alkali-silica reaction damage using acoustic emission: A proof-of-concept study", *Constr. Build. Mater.*, **95**, 406-413. <https://doi.org/10.1016/j.conbuildmat.2015.07.093>.
- Abendroth, M. and Kuna, M. (2003), "Determination of deformation and failure properties of ductile materials by means of the small punch test and neural networks", *Comput. Mater. Sci.*, **28**(3), 633-644. <https://doi.org/10.1016/j.commatsci.2003.08.031>.
- Aggelis, D.G. (2016), *Acoustic Emission Analysis for NDE in Concrete*, Springer, Dordrecht, Netherlands.
- Aker, E., Kühn, D., Vavryčuk, V., Soldal, M. and Oye, V. (2014), "Experimental investigation of acoustic emissions and their moment tensors in rock during failure", *Int. J. Rock Mech. Min. Sci.*, **70**, 286-295. <https://doi.org/10.1016/j.ijrmms.2014.05.003>.
- Benseddiq, N. and Imad, A. (2008), "A ductile fracture analysis using a local damage model", *Int. J. Press. Vessels Pip.*, **85**(4), 219-227. <https://doi.org/10.1016/j.ijpvp.2007.09.003>.
- Chai, M., Zhang, Z., Duan, Q. and Song, Y. (2018), "Assessment of fatigue crack growth in 316LN stainless steel based on acoustic emission entropy", *Int. J. Fatigue*, **109**, 145-156. <https://doi.org/10.1016/j.ijfatigue.2017.12.017>.
- Chou, H., Mouritz, A., Bannister, M. and Bunsell, A. (2015), "Acoustic emission analysis of composite pressure vessels under constant and cyclic pressure", *Compos. Part A-Appl. S.*, **70**, 111-120. <https://doi.org/10.1016/j.compositesa.2014.11.027>.
- Diamanti, K. and Soutis, C. (2010), "Structural health monitoring techniques for aircraft composite structures", *Prog. Aerosp. Sci.*, **46**(8), 342-352. <https://doi.org/10.1016/j.paerosci.2010.05.001>.
- El-Thalji, I. and Jantunen, E. (2015), "A summary of fault modelling and predictive health monitoring of rolling element bearings", *Mech. Syst. Sig. Process.*, **60-61**, 252-272. <https://doi.org/10.1016/j.ymsp.2015.02.008>.
- Elfergani, H.A., Pullin, R. and Holford, K.M. (2013), "Damage assessment of corrosion in prestressed concrete by acoustic emission", *Constr. Build. Mater.*, **40**, 925-933. <https://doi.org/10.1016/j.conbuildmat.2012.11.071>.
- Franklin, A.G. (1969), "Comparison between a quantitative

- microscope and chemical methods for assessment of non-metallic inclusions”, *J. Iron Steel I.*, **207**, 181-186.
- Friesel, M.A. and Carpenter, S.H. (1984), “An inverted strain rate dependence of the acoustic emission generated during the deformation of high purity α -Ti”, *Mater. Sci. Eng.*, **68**(1), 107-111. [https://doi.org/10.1016/0025-5416\(84\)90248-9](https://doi.org/10.1016/0025-5416(84)90248-9).
- Gholizadeh, S., Leman, Z. and Baharudin, B.T.H.T. (2015), “A review of the application of acoustic emission technique in engineering”, *Struct. Eng. Mech.*, **54**(6), 1075-1095. <http://dx.doi.org/10.12989/sem.2015.54.6.1075>.
- Gurson, A.L. (1977), “Continuum theory of ductile rupture by void nucleation and growth: Part I -Yield criteria and flow rules for porous ductile media”, *J. Eng. Mater. Technol.*, **99**, 2-15. <https://doi.org/10.1115/1.3443401>.
- Han, Z., Luo, H. and Wang, H. (2011), “Effects of strain rate and notch on acoustic emission during the tensile deformation of a discontinuous yielding material”, *Mater. Sci. Eng. A*, **528**(13), 4372-4380. <https://doi.org/10.1016/j.msea.2011.02.042>.
- He, M., Li, F. and Wang, Z. (2011), “Forming limit stress diagram prediction of aluminum alloy 5052 based on GTN model parameters determined by in situ tensile test”, *Chin. J. Aeronaut.*, **24**(3), 378-386. [https://doi.org/10.1016/S1000-9361\(11\)60045-9](https://doi.org/10.1016/S1000-9361(11)60045-9).
- Holcomb, D. (1993), “General theory of the Kaiser effect”, *Int. J. Rock Mech. Min.*, **30**(7), 929-935. [https://doi.org/10.1016/0148-9062\(93\)90047-H](https://doi.org/10.1016/0148-9062(93)90047-H).
- Holt, J. and Goddard, D. (1980), “Acoustic emission during the elastic-plastic deformation of low alloy reactor pressure vessel steels I: Uniaxial tension”, *Mat. Sci. Eng.*, **44**(2), 251-265. [https://doi.org/10.1016/0025-5416\(80\)90125-1](https://doi.org/10.1016/0025-5416(80)90125-1).
- Horváth, K., Drozdenko, D., Máthi, K., Bohlen, J. and Dobroň, P. (2016), “Deformation behavior and acoustic emission response on uniaxial compression of extruded rectangular profile of Mg-Zn-Zr alloy”, *J. Alloys Compd.*, **680**, 623-632. <https://doi.org/10.1016/j.jallcom.2016.03.310>.
- James, D.R. and Carpenter, S.H. (1971), “Relationship between acoustic emission and dislocation kinetics in crystalline solids”, *J. Appl. Phys.*, **42**(12), 4685-4697. <https://doi.org/10.1063/1.1659840>.
- Kiran, R. and Khandelwal, K. (2014), “Gurson model parameters for ductile fracture simulation in ASTM A992 steels”, *Fatigue Fract. Eng. M.*, **37**(2), 171-183. <https://doi.org/10.1111/ffe.12097>.
- Kumar, J., Punnose, S., Mukhopadhyay, C.K., Jayakumar, T. and Kumar, V. (2012), “Acoustic emission during tensile deformation of smooth and notched specimens of near alpha titanium alloy”, *Res. Nondestr. Eval.*, **23**(1), 17-31.
- McClintock, F.A. (1968), “A criterion for ductile fracture by the growth of holes”, *J. Appl. Mech.*, **35**(2), 363-371. <https://doi.org/10.1115/1.3601204>.
- Mi, C., Buttry, D.A., Sharma, P. and Kouris, D.A. (2011), “Atomistic insights into dislocation-based mechanisms of void growth and coalescence”, *J. Mech. Phys. Solids*, **59**(9), 1858-1871. <https://doi.org/10.1016/j.jmps.2011.05.008>.
- Montgomery, D.C. (2013), *Design and Analysis of Experiments*, (8th Edition), John Wiley & Sons, New York, NY, USA.
- Moorthy, V., Jayakumar, T. and Raj, B. (1995), “Acoustic emission technique for detecting micro- and macroyielding in solution-annealed AISI Type 316 austenitic stainless steel”, *Int. J. Press. Vessels Pip.*, **64**(2), 161-168. [https://doi.org/10.1016/0308-0161\(94\)00154-B](https://doi.org/10.1016/0308-0161(94)00154-B).
- Mukhopadhyay, C.K., Jayakumar, T., Raj, B. and Ray, K.K. (2007), “Acoustic emission during tensile deformation of pre-strained nuclear grade AISI Type 304 stainless steel in the unnotched and notched conditions”, *J. Mater. Sci.*, **42**(14), 5647-5656. <https://doi.org/10.1007/s10853-006-1273-3>.
- Myers, R.H., Montgomery, D.C. and Anderson-Cook, C.M. (2012), *Response Surface Methodology: Process and Product Optimization Using Designed Experiments*, (4th Edition), Wiley, New York, NY, USA.
- Nair, A. and Cai, C. (2010), “Acoustic emission monitoring of bridges: Review and case studies”, *Eng. Struct.*, **32**(6), 1704-1714. <https://doi.org/10.1016/j.engstruct.2010.02.020>.
- Njuhovic, E., Bräu, M., Wolff-Fabris, F., Starzynski, K. and Altstädt, V. (2015), “Identification of failure mechanisms of metallised glass fibre reinforced composites under tensile loading using acoustic emission analysis”, *Compos. Part B-Eng.*, **81**, 1-13. <https://doi.org/10.1016/j.compositesb.2015.06.018>.
- Oral, A., Anlas, G. and Lambros, J. (2012), “Determination of Gurson-Tvergaard-Needleman model parameters for failure of a polymeric material”, *Int. J. Damage Mech.*, **21**(1), 3-25. <https://doi.org/10.1177%2F1056789510385261>.
- Qiu, F., Dai, G. and Zhang, Y. (2017), “Application of an acoustic emission quantitative method to evaluate oil tank bottom corrosion based on corrosion risk pace”, *Brit. J. Nondestr. Test.*, **59**(12), 653-658. <https://doi.org/10.1784/insi.2017.59.12.653>.
- Rehman, S.K.U., Ibrahim, Z., Memon, S.A. and Jameel, M. (2016), “Nondestructive test methods for concrete bridges: A review”, *Constr. Build. Mater.*, **107**, 58-86. <https://doi.org/10.1016/j.conbuildmat.2015.12.011>.
- Rice, J. and Tracey, D. (1969), “On the ductile enlargement of voids in triaxial stress fields”, *J. Mech. Phys. Solids*, **17**(3), 201-217. [https://doi.org/10.1016/0022-5096\(69\)90033-7](https://doi.org/10.1016/0022-5096(69)90033-7).
- Springmann, M. and Kuna, M. (2005), “Identification of material parameters of the Gurson-Tvergaard-Needleman model by combined experimental and numerical techniques”, *Comp. Mater. Sci.*, **33**(4), 501-509. <https://doi.org/10.1016/j.commatsci.2005.02.002>.
- Springmann, M. and Kuna, M. (2006), “Determination of ductile damage parameters by local deformation fields: Measurement and simulation”, *Arch. Appl. Mech.*, **75**(10), 775-797. <https://doi.org/10.1007/s00419-006-0033-9>.
- Tang, C. (1990), “Evolution and propagation of material defects and Kaiser effect function”, *J. Seismol. Res.*, **13**(2), 203-213.
- Tvergaard, V. and Needleman, A. (1984), “Analysis of the cup-cone fracture in a round tensile bar”, *Acta Metall.*, **32**(1), 157-169. [https://doi.org/10.1016/0001-6160\(84\)90213-X](https://doi.org/10.1016/0001-6160(84)90213-X).
- Uthaisangsuk, V., Prahl, U., Münstermann, S. and Bleck, W. (2008), “Experimental and numerical failure criterion for formability prediction in sheet metal forming”, *Comp. Mat. Sci.*, **43**(1), 43-50. <https://doi.org/10.1016/j.commatsci.2007.07.036>.
- Wang, L.Y. and Li, L. (2017), “Parameter identification of GTN model using response surface methodology for high-strength steel BR1500HS”, *J. Mater. Eng. Perform.*, **26**(8), 3831-3838. <https://doi.org/10.1007/s11665-017-2806-4>.
- Yu, J., Ziehl, P., Zárate, B. and Caicedo, J. (2011), “Prediction of fatigue crack growth in steel bridge components using acoustic emission”, *J. Constr. Steel Res.*, **67**(8), 1254-1260. <https://doi.org/10.1016/j.jcsr.2011.03.005>.
- Zanganeh, M., Pinna, C. and Yates, J.R. (2013), “Void growth and coalescence modelling in AA2050 using the Rousselier model”, *Int. J. Damage Mech.*, **22**(2), 219-237. <https://doi.org/10.1177/1056789512441808>.
- Zhang, K., Hua, L., Zheng, C. and Radon, J. (1989), “A computer simulation of ductile fracture initiation in TPB specimen: An application of V_{gc} criterion”, *Eng. Fract. Mech.*, **33**(5), 671-677. [https://doi.org/10.1016/0013-7944\(89\)90065-9](https://doi.org/10.1016/0013-7944(89)90065-9).
- Zhang, Z.L. and Skallerud, B. (2010), “Void coalescence with and without prestrain history”, *Int. J. Damage Mech.*, **19**(2), 153-174. <https://doi.org/10.1177%2F1056789508101919>.
- Zhong, J., Xu, T., Guan, K. and Zou, B. (2016), “Determination of ductile damage parameters using hybrid particle swarm optimization”, *Exp. Mech.*, **56**(6), 945-955. <https://doi.org/10.1007/s11340-016-0141-6>.
- Zou, S., Yan, F., Yang, G. and Sun, W. (2017), “The identification

of the deformation stage of a metal specimen based on acoustic emission data analysis”, *Sensors*, **17**(4), 789(1-13).
<https://doi.org/10.3390/s17040789>.

CC